Special Collection on "**Testing and Modeling on Particle Breakage for Granular Soils (Yang Xiao, Chandrakant S. Desai, Hanlong Liu)**

Crushing and Flooding Effects on One-dimensional Time-dependent Behaviors of a Granular Soil

Wen-Bo Chen; Kai Liu; Zhen-Yu Yin; and Jian-Hua Yin

Abstract: Particle crushing contributes significantly to the time-dependent compression behaviors of crushable granular soils. It is also widely accepted that flooding would aggravate the breakage level of soil particles. This study aims to investigate the combined behavior. A crushable granular soil was chosen to preform one-dimensional compression tests, i.e., constant-rate of strain tests and multistage loading oedometer tests, under dry and saturated conditions. Besides, the crushing mechanism of particles was investigated by measuring the microhardness of soil particles. Furthermore, the shape characteristics (circularity, aspect ratio, roundness and solidity) of particles before and after tests were analyzed by digital image processing (DIP) method. The results show that the “isotach” behavior is observed for the tested soil in saturated condition. The compression curve, creep behavior and level of particle breakage of initially dry specimens would evolve to the same manner in which the initially saturated specimens behave. The microhardness test clearly has attributed the breakage of particles to the disaggregation of clay minerals which are the bonding materials between micro- quartz particles. This disaggregation became more severe after the moisturization of soil particles. The plastic work done to each specimen and corresponding breakage ratio are correlated by two hyperbolic functions, which define two characteristic curves for dry and saturated/flooded conditions. The results from DIP analysis indicate that the average values of shape descriptors of all the particles in one specimen would change during compression, with a larger level under saturated or flooded condition than under dry condition.

Keywords: granular soil, particle breakage, flooding, time-dependency, particle shape, compression.

Wen-Bo Chen,

Ph. D. Candidate, Department of Civil and Environmental Engineering, The Hong Kong Polytechnic University, Hung Hom, Kowloon, Hong Kong, China.

Email: geocwb@gmail.com

Kai Liu

Ph. D. Candidate, Department of Civil and Environmental Engineering, The Hong Kong Polytechnic University, Hung Hom, Kowloon, Hong Kong, China.

Email: kevin-kai.liu@connect.polyu.hk

Zhen-Yu Yin (Corresponding Author)

Associate Professor, Department of Civil and Environmental Engineering, The Hong Kong Polytechnic University, Hung Hom, Kowloon, Hong Kong, China.

Email: zhenyu.yin@polyu.edu.hk; zhenyu.yin@gmail.com

Jian-Hua Yin

Chair Professor, Department of Civil and Environmental Engineering, The Hong Kong Polytechnic University, Hung Hom, Kowloon, Hong Kong, China.

Email: cejhyin@polyu.edu.hk

Introduction

For granular soils, particle breakage contributes significantly to their time-dependent compression behaviors, including strain-rate effect, creep, and stress relaxation. Extensive studies on the particle breakage of granular soils have been conducted using conventional oedometer, constant-rate of strain test or triaxial test (Yamamuro et al. 1996; Ueng and Chen 2000; Takei et al. 2001; Augustesen et al. 2004; Lade and Karimpour 2010, 2014, 2016; Lade et al. 2010; Kikkawa et al. 2012; Chen et al. 2016; Hyodo et al. 2016; Lv et al. 2017; Xiao and Liu 2017; Yin et al. 2017a; Chen et al. 2018; Chen et al. 2019a, 2019b; Xiao et al. 2019b; Xu et al. 2019). Furthermore, by means of numerical simulation based on discrete element method, several researchers have investigated the micro-scale mechanisms of particle breakage (Couroyer et al. 1999; Silvani et al. 2009; Kwok and Bolton 2013; McDowell et al. 2013; McDowell and De Bono 2013; Cil and Buscarnera 2016; Fu et al. 2017; Xiong et al. 2017; Manso et al. 2018; Xiong et al. 2018; Zhou et al. 2018). More recently, X-ray tomography (Goodwin et al. 2003; Karatza et al. 2017; Guida et al. 2018), infrared thermography (Salami et al. 2017), and acoustic emission technique (Li et al. 2018) have been adopted to study the particle breakage in a more visualized and quantitative way.

Fewer investigations focused particularly on the effect of flooding on particle breakage of crushable granular soils. Karimpour et al. (2010) observed that the sand particles were more brittle in the presence of water. A unique relationship between strain, stress, total suction and time for creep of compacted rockfill was proposed and validated by Oldecop and Alonso (2007). Ovalle et al. (2015) reported that after flooding, the dry granular soils possessed equivalent behaviors of initially wetted soils in terms of compression curve and the level of particle crushing. Generally, a consensus has been reached on that flooding would reduce the inter-particle friction or interlocking, weaken the particle strength, and accelerate the static fatigue of particle, thereby inducing excessive compression deformation (Shi and Herle 2017; Shi et al. 2018a). This

78 negative effect is particularly crucial for crushable granular soils.
79
80 For cohesive soils, like clay, a unique stress-strain-strain rate relationship has been
81 found (Bjerrum 1967; Yin and Graham 1989, 1994, 1999; Cheng and Yin 2005; Yin et
82 al. 2011, 2014, 2015; Wang and Yin 2015; Zhu et al., 2016; Yin et al. 2017b; Shi et al.
83 2018b, Jin et al. 2019), which indicates that it is possible to establish a clear correlation
84 between strain-rate effect, creep and stress relaxation behavior. For granular soils,
85 however, all these three time-dependent phenomena should be investigated separately
86 because no definite correlations between them can be found (Lade and Karimpour
87 2010). Few existing studies have covered all these three behaviors of one particular
88 granular soil. Besides, a development of interlocking or cementation between particles
89 with time, named “structuration”, is widely recognized for granular soils (Augustesen
90 et al. 2004). Importantly, the majority of the adopted testing material is silica sand or
91 rock material which is less sensitive to water content change and relatively difficult to
92 crush. Therefore, full time-dependencies (i.e. strain-rate effect, creep, and stress
93 relaxation) of crushable granular soils combined with flooding effect remain to be
94 systematically investigated.
95
96 In the current study, a crushable granular soil with relatively low particle strength was
97 adopted as testing material. Constant-rate of strain (CRS) and multistage loading
98 oedometer (MLO) tests on different specimens with various moisture conditions were
99 performed to investigate the time-dependent behaviors in one-dimensional condition
100 with effect of flooding. Importantly, the deformation mechanism at particle scale was
101 discussed by evaluating the microstructure and microhardness of soil particles. The
102 change in particle size distribution (PSD) curves before and after tests were correlated
103 with plastic work. Furthermore, considering the significant influence of particle shape
104 on the mechanical behavior of soils (Xiao et al. 2019a), four representative shape
105 descriptors (circularity, aspect ratio, roundness and solidity) of soil particles before and

after tests were determined and analyzed by digital image processing (DIP) techniques.

Experimental investigation

Tested material

The tested granular soil was a portion of fill material used in a pavement construction site. The gradation was rather uniform so that the breakage would be enhanced and identifiable changes in the gradation curve were more likely to occur. The characteristic indices of this soil are summarized as follows: minimum diameter (d_{min}), 2 mm; maximum diameter (d_{max}), 5 mm; mean diameter (d_{50}), 3.298 mm; coefficient of uniformity (C_u), 1.605; coefficient of curvature (C_c), 0.942; specific gravity (G_s), 2.63; maximum void ratio (e_{max}), 1.176; the minimum void ratio is not applicable here due to the high crushability of the particles. The typical particles are shown in Fig. 1(a).

Testing apparatus

Following the recommendation of Head (1985), a steel oedometer ring with an internal diameter of 82.55 mm was designed and manufactured as the confining ring for both CRS and MLO tests. As shown in Fig. 2(a), The loading frame of standard triaxial compression machine was adopted. The vertical load and vertical deformation of the specimen were measured by an S-beam load cell and a linear variable differential transducer (LVDT), respectively. As for the MLO tests (Fig. 2(b)), the vertical load on the specimen was applied by lever-magnified dead weight. Similarly, an LVDT was adopted for measuring the vertical deformation. Drainage was only allowed at the top of the specimen. Due to the high void ratio and high permeability of this tested material, no pore water pressure transducer was used, and thus the total vertical stress is assumed to be the effective vertical stress (σ'_v). All the transducers were carefully calibrated, and the possible errors induced by the deformations of the loading frame and load cell were well considered and corrected in the data analysis. The microhardness measurements were implemented with a digital Vickers microhardness tester (HVX-1000A, China).

The photos of particles for DIP analysis were taken using Canon EOS 700D camera with a capacity of 18 million effective pixels.

Testing program

The testing program is listed in detail in Table 1. To minimize the probability that the soil particles crushed during the specimen preparation, the specimens were prepared at loose state. Firstly, the air-dried granular soil of 310 g in total was equally divided into four batches. Then, four batches of soil were poured into the ring from the same height in sequence and were gently tapped by a rubber hammer at each layer. The void ratios for all specimens were kept at 0.857±0.01. The air-dried granular soils were reserved in the laboratory with a temperature of 20±1 ℃and almost constant humidity of around 55% for more than one year. For the saturated specimens, the prepared specimens were submerged under water, and a vacuum pressure of -100 kPa was applied for 12 hours before testing. It is worth noting that the so-called "saturated" here represents an approximately saturated condition, because it is difficult to achieve fully saturated condition under -100 kPa vacuum pressure within 12 hours and difficult to determine the accurate saturation degree which influences the crushability of grains (Ovalle et al. 2015). Note that in this study, the saturation procedure was kept identical for all the saturated specimens to make sure the saturation degree constant. For the flooded specimens, deaired water was added into initially-dry specimens at a certain phase of the test, as shown in Table 1. Besides, the strain rate ($\dot{\varepsilon}$) was varied at three levels (0.2%/h, 2%/h and 20%/h) in the CRS tests, and the maximum vertical stress was controlled at 2 MPa for all specimens. To eliminate the effect of loading period on the test results from MLO and CRS tests, the time point for applying each vertical stress in MLO test was kept same as that needed for the CRS test with strain rate of 2%/h to reach the same level of vertical stress.

Several typical soil particles were chosen, then dipped and fixed in epoxy to form a

sliced cylindrical specimen. The surface of the specimen was polished carefully following the procedures adopted by Zhan et al. (2018) until the cross-sections of soil particles were well exposed to air. After 10 days' drying in the air, the first series of microhardness measurements was performed. Subsequently, the specimen was submerged in the deaired water and held under a -100 kPa vacuum pressure for 12 hours. The second series of measurements was performed on the same soil particles in the specimen immediately after the specimen was taken out from water. To ensure that no moisture is lost during the process, deaired water was spread on the surface of specimen after each indentation to keep the particle surface always moistened.

The particle shape analysis by DIP was only implemented on the particles retained on sieve #30 (d>0.6 mm). Due to the large number of particles, all the particles were divided into several batches in the image acquisition stage and analyzed collectively in the analysis stage. As shown in Fig. 1(a), all particles in one batch were arranged without touching and overlapping with each other. The image analysis was conducted using ImageJ software (NIH, USA) (Xiao et al. 2019a). The analysis consists of four procedures including scale setting, binary image generation, image processing and particle analysis. Firstly, pixel values on each image were converted into millimeter by scale factors. Then, original images (Fig 1(a)) were converted into binary images (Fig 1(b)) for analysis. Followingly, several steps including Dilate, Fill holes and Erode processes were carefully carried out to make sure no addition or removal of pixels from the real particles (Ferreira and Rasband 2012; Kumara et al. 2012). Four shape descriptors (circularity, aspect ratio, roundness, and solidity) of every particle were calculated automatically by the software, and the calculation formula for each descriptor is listed in Table 2. Gather all the calculated shape descriptors information from all the particles to form a database for one specimen. Then, the database is imported to the data analysis software Origin. The value range of shape descriptor is divided into small sections. Each soil particle will be grouped into one specific section

based on their descriptor value. Lastly, the number of soil particles in each small section will be counted by the Origin automatically.

Results and interpretation

Compression behaviors

Fig. 3 plots the compression curves of the granular soil in the CRS and MLO tests under dry and saturated conditions. To ease the comparison, the fitting equations of corresponding curves are also presented in Fig. 3. It demonstrates that the compression curves from CRS and MLO tests match well with each other, although some minor gaps can be observed. This implies that a good repeatability of the tests has been achieved. For the specimens under both dry and saturated conditions, the slopes of the compression curve at the beginning are several times steeper than the unloading-reloading index (C_s, the slope of the unloading-reloading line in e-log(σ'_v) plane). This can be explained by two concurrent mechanisms: (a) the crushable particles starting to crush even at the low levels of vertical stresses during the initial loading (Ovalle et al. 2015), and (b) rearrangements of particles by sliding and rotation for the loosely-compacted specimens. The increase of water content remarkedly reduces the deformation resistance of the specimens. The compression index (C_c, the slope of the normal compression line in e-log(σ'_v) plane) for the saturated specimens is 1.71 times larger than that for the dry specimens. In addition, at the same level of stress, the elastic deformations of the saturated specimen in the unloading-reloading period are larger than those of the dry specimen. Despite the fact that the particles breakage could possibly occur from the beginning of loading, the yielding stress (σ'_y), as marked in Fig. 3, is normally regarded as an indication of the onset of particle crushing. Under the same moisture condition, the yielding stresses from CRS test, $\sigma'_{y,CRS}$, and that from MLO test, $\sigma'_{y,MLO}$ differ slightly. It reveals that the compression behaviors acquired from MLO and CRS tests could be similar provided that the strain rate is kept at the same level. The effect of moisture content of the specimen on the crushing resistance

is obvious, with the average σ'_y from CRS and MLO tests decreasing significantly by 51.8% when the specimen is changed from dry to saturated condition.

Time-dependencies

Fig. 4 presents the time-dependencies (i.e. strain-rate effect, creep, and stress relaxation) of the crushable granular soils in MLO and CRS compression tests under dry and saturated conditions.

Fig. 4(a) shows that at a certain void ratio, the higher strain rate, the higher effective vertical stress. The commonly acknowledged concept of "isotach" (unique σ'_v-ε-$\dot{\varepsilon}$ relationship) for clayey soils seems is only valid for the soil specimen under saturated condition and does not apply for the specimen under dry condition. Furthermore, this finding is inconsistent with the test results on granular soils in some previous studies (e.g. Karimpour and Lade 2010; Lade and Karimpour 2010), which reported that the strain rate only had a temporary effect on the compression curve (i.e. the stress-strain relation would gradually rejoin a unique relationship after the change of strain rate). This difference is possibly due to the differences in the crushability of soil particles and the stress range of interest. As shown in Fig. 4(b), after 1.67 mins (100 seconds) of loading, the relationship between void ratio and the logarithm of time is almost linear. Under identical effective vertical stresses, the fitted creep coefficients (C_t, based on e-log(t) curve) of the dry specimen are lower than those of the saturated one. Similarly, as shown in Fig. 4(c), the stress relaxation coefficient (R_α, based on σ'_v-log(t) curve) of dry specimen is lower than that of the saturated one. These results imply that the increase of moisture content strengthens the time-dependency of the deformation behaviors of crushable granular soils.

Flooding effect

The flooding effects on the creep, stress relaxation and compression behaviors of

crushable granular soil are shown in Fig. 5. It can be seen from Fig. 5(a) that the curve of MLO_Flo initially creeps consistently with that of MLO_Dry. After creeping for 1 hour, the water was added into the specimen, and the void ratio immediately drops down towards the creep curve of the saturated specimen that is under identical effective vertical stress. The specimen turned into a conditionally stable state at 24 mins after the addition of water, and a sudden drop of void ratio occurred at around 600 mins later. Then, the flooded specimen was incrementally applied to 2000 kPa. It can be observed that the creep curve of flooded specimen practically rejoins and overlaps the curve of the saturated specimen. Fig. 5(b) presents the test results from two stress relaxation tests with different starting time points of adding water. The stress relaxation curves of all initially dry specimens are almost identical. As shown in the figure, immediately after the addition of water, the effective vertical stress dramatically reduces to a low level and quickly turns into decreasing in a linear relationship with the logarithm of time. Note that the effective vertical stress drops suddenly by a large amplitude after adding water so that the apparatus unexpectedly compressed the specimen to supplement the sudden drop of the load. The levels of unexpected compression are slightly different for CRS_Flo1 and CRS_Flo2. Therefore, the stress relaxation tests of flooded specimen were not implemented under a strictly constant strain level, which complicates the discussion of this phenomenon. Note that more tests are needed to clarify the relationships between the stress relaxation behaviors under dry, saturated and flooded specimens. In Fig. 5(c), the compression curve of MLO_Flo specimen initially follows that of MLO_Dry, and then gradually converges to that of the MLO_Sat after flooding at effective vertical stress of 500 kPa. As shown in Fig. 5(d), the compression curves of two initially dry specimens in CRS condition overlap with each other. The stress relaxation was followed by compression at a $\dot{\varepsilon}$ of 2%/h until 2000 kPa was reached. A slight overshooting of the effective vertical stress after recompression is observed in the figure, which can be explained by the “structuration” occurred during stress relaxation. With the further increase of effective vertical stress, the compression curve

of CRS_Flo2 gradually evolves in the manner of CRS_Sat.

Crushing effect

A particle-scale investigation is a basis for considering the crushing effect on macroscopic deformation. Measuring microhardness is a commonly used approach for characterizing the properties of the minerals and it shows certain correlation with the strength of the particles (Igarashi et al. 1996). Fig. 6 presents a typical microscopic view of a well-polished cross-section of a single grain of soil particle for microhardness measurement and the typical indentation points. It can be seen that a single grain of test soil particle comprises of micro- angular particles (bright areas) and the bonding materials (dim areas). 10-grams and 100-grams loads were, respectively, used for indenting the surfaces of five randomly-chosen micro- particles and five sections of bonding materials (Xuan et al. 2009; Xuan et al. 2016). The measurements were repeated for dry and saturated specimens. Figs. 6(b) and 6(c) show the typical indentations on bright angular particles and bonding materials. As shown in Fig. 7, when the soil particles are air-dried, the average Vickers microhardness (VM) value of bright particles is 1387.1 kg/mm^2, contrasting with 66.5 kg/mm^2 for the bonding materials. Besides, X-ray fluorescence (XRF) test was conducted on the tested soil particles. The results show that the percentages by mass of SiO_2, Al_2O_3, Fe_2O_3, and MgO are 62.3%, 19.3%, 5.25% and 4.58%, respectively. Therefore, it is reasonable to speculate that the bright angular particles and bonding materials are quartz and clay minerals, respectively, based on the VM values (Samsonov 2012) and the percentages of oxide components. After saturation, the VM values of quartz particles has a negligible drop of 5.0%, while the drop is up to 65.0% for the clay mineral. Therefore, it can be concluded that, for the tested granular soil, particle crushing is mainly induced by the disaggregation of clay minerals, which could be further significantly aggravated due to the increase of moisture content.

The particle size distribution curves of the specimens after tests were determined by mechanical sieving, as shown in Fig. 8. The breakage ratio (B_r), varying from 0 to 1, can be determined by the following formulation proposed by Einav (2007):

$$F(d) = (1 - B_r) F_0(d) + B_r F_u(d) \quad (1)$$

where $F(d)$, $F_0(d)$ and $F_u(d)$ are current, initial and fractal PSDs, respectively, with $F_u(d) = (d / d_{\max})^{0.3}$ (Coop et al. 2004). It is clear that the larger the B_r, the higher the level of breakage. The calculated B_r values for all specimens are listed in Table 3. Taking tests CRS_Dry and CRS_Sat as the references which are tested under dry and saturated conditions, respectively, without experiencing creep. With the comparison on B_r values between the references and tests MLO_Dry and MLO_Sat, it can be concluded that creep can enhance the breakage level in both dry and saturated conditions, thereby proving that particle crushing of granular soils under constant stress is a time-dependent behavior (Augustesen et al. 2004; Oldecop and Alonso 2007; Karimpour and Lade 2010). As expected, the B_r values are very sensitive to the change of water content. Similar observations for decomposed granite and carbonate sand were reported by Lee and Coop (1995). The reason behind has been explained in detail at the particle scale in the previous paragraph.

Several researchers (Daouadji and Hicher 2010; Ovalle et al. 2015; Hu et al. 2018; Jin et al. 2018a, 2018b) have stated that the B_r increases monotonically with increasing plastic work (w_p) under a certain moisture content, provided that the initial void ratio and PSD are kept identical. To reach the same level of breakage, larger plastic work is required for dry specimen than the moisturized specimen. The level of particle breakage (B_r) is usually expressed as:

$$B_r = \frac{w_p}{a + w_p} \quad (2)$$

where a is a fitting parameter, that is assumed as a constant for the soil specimen under

328 one certain moisture content. The plastic work was calculated as the sum of all
329 increments of the total work done in compression, minus the elastic work done in the
330 unloading period. All the increments of work are calculated as the product of the
331 average vertical stress and the vertical strain occurs during two adjacent measuring time
332 points. Note that the plastic work in dry condition ($w_{p,d}$) and the plastic work in
333 saturated or flooded condition ($w_{p,w}$) should be calculated separately. The calculated
334 values of plastic work are listed in Table 3. More energy dissipation is needed in a dry
335 specimen to reach a given PSD, compared with saturated or flooded specimen.
336 Therefore, for the flooded specimens, the B_r value initially rose up following the trend
337 of dry specimens (the blue line in the Fig. 9) to a certain level of breakage, $B_{r,1}$. After
338 they are flooded, the breakage value will develop from $B_{r,1}$ to the final $B_{r,f}$ along the
339 trend of the saturated condition (the red line in the Fig. 9).
340
341 If the plastic work values needed for a dry and a saturated specimens to reach a breakage
342 value of $B_{r,1}$ are expressed as $W_{p,d1}$ and $W_{p,w1}$, respectively, then we can have

343 $$\frac{W_{p,d1}}{a_1 + W_{p,d1}} = \frac{W_{p,w1}}{a_2 + W_{p,w1}} \tag{3}$$

344 where a_1 and a_2 are the fitting parameters for dry and saturated specimens, respectively.
345 From Eq. (3), we can get

346 $$W_{p,w1} = W_{p,d1} \cdot \frac{a_2}{a_1} \tag{4}$$

347 If the plastic work after flooding is denoted as $W_{p,w2}$, then the final $B_{r,f}$ can be expressed
348 as

349 $$B_{r,f} = \frac{W_{p,w2} + W_{p,d1} \cdot \frac{a_2}{a_1}}{a_2 + W_{p,w2} + W_{p,d1} \cdot \frac{a_2}{a_1}} \tag{5}$$

350 If $W_{p,w2} + W_{p,d1} \cdot \frac{a_2}{a_1}$ is taken as "equivalent plastic work", $W_{p,e}$, Eq. (5) can be written
351 as

$$B_{r,f} = \frac{W_{p,e}}{a_2 + W_{p,e}} \quad (6)$$

The $W_{p,e}$ presents the plastic work that needed for the saturated specimen to reach the same breakage level that a flooded specimen achieves. If no flooding happens, $W_{p,e}$ is equal to $W_{p,d}$ for dry specimen and is equal to $W_{p,w}$ for saturated specimen.

Based on all the tests, parameters of a for the dry and saturated conditions were fitted as 320.0, and 174.1 respectively. The calculated breakage ratio for each test using the fitted parameters are also listed in Table 3. Fig. 9 presents the relationships of B_r and $w_{p,e}$ at the end of each test and the fitting curves, which are nearly parallel to each other in the figure.

Particle shape analysis by DIP

Four standard shape descriptors of each individual particle were automatically calculated by ImageJ. Fig. 10 demonstrates the histograms and fitted normal distribution curves of the circularity versus corresponding particle number under CRS and MLO test conditions. As shown in Fig. 10(a), for CRS specimens, the increase of average circularity of particles under saturated or flooded condition is larger than that under dry conditions. This indicates the compression under the wet conditions renders particle assembling a perfect circle. As shown in Figure 10(b), the increased water content has less influence on the circularity change for the particles under MLO condition than those under CRS condition. The different trends for two test conditions may attribute to the different stress paths in the tests. Under both CRS and MLO loading methods, the circularity values change within a range of 0.5 to 1. The histograms and fitted normal distribution curves for the aspect ratio versus corresponding particle number are plotted in Fig. 11. As shown in Fig. 11(a), for CRS specimens, in both wet and dry conditions, compression has caused a greater average aspect ratio of particles. The wide normal distribution curve of the CRS_Dry specimen highlights that it has a

wider range of aspect ratio than that of other specimens. Besides, the increase of average aspect ratio under the wet condition is greater than that under dry condition. The similar trend was also observed for MLO specimens. Under both CRS and MLO test conditions, the average aspect ratios of all particles range from 1 to 2.2. Fig. 12 shows the histograms and fitted normal distribution curves for the roundness versus corresponding particle number under different test conditions. It can be seen that the average roundness is not sensitive to water content and the change of test condition, getting lower under both the dry and wet conditions compared with that of original state. The average roundness of all particles under different test conditions distributes in a range from 0.5 to 1. The histograms and fitted normal distribution curves for the solidity versus corresponding particle number are plotted in Fig. 13. The compression lowers down the average solidity of particles, especially for the specimens under saturated or flooded condition. This trend indicates the surfaces of particles, in general, become more corrugated compared with the soil particles polished naturally. It is also observed that the different test conditions have slight effects on the solidity of particles. The solidity values for all the particles change from 0.8 and 1.

Conclusions

In this study, four constant-rate of strain tests and three multistage loading oedometer tests were conducted on a crushable granular soil under dry, saturated, or flooded condition. Microhardness tests were implemented to explain the crushing mechanism at particle scale under dry or wet condition. Digital image processing technique was also utilized in order to investigate the changes in particle shape of soil particles before and after the tests. The following conclusions can be drawn:

(a) The tested crushable soil particles start to crush even under low levels of vertical stress. The presence of water significantly weakens the compression resistance of

405 the soil specimen.
406 (b) At a certain void ratio, the vertical stress on the specimen exhibits a strain-rate
407 dependency, however, the “isotach” behavior seems is only valid for the saturated
408 specimen and a unique characteristic curve for stress and void ratio are not observed
409 for the tested soil. Both the creep coefficient and stress relaxation coefficient of the
410 dry specimens are smaller than that of the saturated ones.
411 (c) The saturated specimen and the flooded specimen share the same behaviors in terms
412 of creep and stress-strain relationship under compression. However, regarding
413 stress relaxation behavior, the flooded specimens showed much smaller stress
414 relaxation coefficients than that of the saturated specimen. This can be possibly
415 explained by the stress level, at which relaxation and flooding start, is too high for
416 the tested crushable granular soil so that the sudden collapse induced by
417 moisturization exerts a severe destructive effect on the soil structure.
418 (d) By measuring the local microhardness on a single grain of soil particle, it is
419 observed that the soil particle comprises of micro- quartz particles and clay minerals,
420 whose microhardness and strength would drop greatly due to the increase of water
421 content, thereby aggravating particle breakage.
422 (e) The breakage ratio of the specimen can be well correlated with the equivalent plastic
423 work done during the compression. Two fitted curves for dry and saturated/flooded
424 conditions, respectively, are almost parallel in the plot of breakage ratio with respect
425 to the logarithm of equivalent plastic work.
426 (f) The increase of water content would facilitate the change in shape of soil particles.
427 The compression generally renders the particles assembling a circle, meanwhile
428 being more corrugated on the surfaces.
429
430 It is recommended that the full time-dependencies of crushable granular material should
431 be investigated under triaxial, even hollow cylinder test conditions to investigate the
432 effect of more complicated stress paths.

Data Availability

All data, models, and code generated or used during the study appear in the submitted article.

Acknowledgement

This research was financially supported by the National Natural Science Foundation of China (Grant No. 51579179). In addition, the authors thank Dr. Xuan Dongxing, Dr. Zhan Baojian, and Miss Ruan Fei for their kind helps in the tests.

References

Arasan, S., Akbulut, S., and Hasiloglu, A. S. (2011). "Effect of particle size and shape on the grain-size distribution using Image analysis." *International journal of civil and structural engineering*, 1(4), 968-985.

Augustesen, A., Liingaard, M., and Lade, P. V. (2004). "Evaluation of time-dependent behavior of soils." *Int. J. Geomech*., 4(3), 137-156.

Chen, Q., Indraratna, B., Carter, J. P., Nimbalkar, S., (2016). "Isotropic-kinematic hardening model for coarse granular soils capturing particle breakage and cyclic loading under triaxial stress space." *Can. Geotech. J.*, 53(4), 646-658.

Chen, W. B., Feng, W. Q., Yin, J. H., Borana, L., and Chen, R. P. (2019a). "Characterization of permanent axial strain of granular materials subjected to cyclic loading based on shakedown theory." *Constr Build Mater*, 198, 751-761.

Chen, W. B., Liu, K., Feng, W. Q., Borana, L., and Yin, J. H. (2019b). "Influence of matric suction on nonlinear time-dependent compression behavior of granular fill material." *Acta Geotech.*, https://doi.org/10.1007/s11440-018-00761-y

Chen, W. B., Yin, J. H., Feng, W. Q., Borana, L., and Chen, R. P. (2018). "Accumulated permanent axial strain of a subgrade fill under cyclic high-speed railway loading." *Int J Geomech*, 18(5), 04018018.

Cheng, C. M., and Yin, J. H. (2005). "Strain-Rate Dependent Stress--Strain Behavior of Undisturbed Hong Kong Marine Deposits under Oedometric and Triaxial Stress States." *Mar. Georesour. Geotec.*, 23(1-2), 61-92.

Cil, M. B., and Buscarnera, G. (2016). "DEM assessment of scaling laws capturing the grain size dependence of yielding in granular soils." *Granul. Matter*, 18(3), 36.

Coop, M. R., Sorensen, K. K., Bodas Freitas, T., and Georgoutsos, G. (2004). "Particle breakage during shearing of a carbonate sand." *Géotechnique*, 54(3), 157-163.

Couroyer, C., Ning, Z., Ghadiri, M., Brunard, N., Kolenda, F., Bortzmeyer, D., and Laval, P. (1999). "Breakage of macroporous alumina beads under compressive loading: simulation and experimental validation." *Powder Technol.*, 105(1-3), 57-

65.

Daouadji, A., and Hicher, P. Y. (2010). “An enhanced constitutive model for crushable granular materials.” *Int. J. Numer. Anal. Methods Geomech.*, 34(6), 555–580.

Einav, I. (2007). “Breakage mechanics-Part I: Theory.” *J. Mech. Phys. Solids*, 55(6), 1274–1297.

Ferreira, T., and Rasband, W. (2012). “ImageJ user guide”. ImageJ/Fiji, 1.

Fu, R., Hu, X., and Zhou, B. (2017). “Discrete element modeling of crushable sands considering realistic particle shape effect.” *Comput. Geotech.*, 91, 179-191.

Goodwin, A. K., O'Neill, M. A., and Anderson, W. F. (2003). “The use of X-ray computer tomography to investigate particulate interactions within opencast coal mine backfills.” *Eng. Geol.*, 70(3-4), 331-341.

Guida, G., Casini, F., Viggiani, G. M. B., Andò, E., and Viggiani, G. (2018). “Breakage mechanisms of highly porous particles in 1D compression revealed by X-ray tomography.” *Géotech. Lett.*, 8(2), 155-160.

Head, K. H. (1985). “Manual of soil laboratory testing: Effective stress tests.” Vol. 3, 1129-1225. London: Pentech Press.

Hu, W., Yin, Z. Y, Scaringi, G., Dano, C., and Hicher, P. Y. (2018). “Relating fragmentation, plastic work and critical state in crushable rock clasts.” *Eng. Geol.*, 246, 326-336.

Hyodo, M., Wu, Y., Aramaki, N., and Nakata, Y. (2016). "Undrained monotonic and cyclic shear response and particle crushing of silica sand at low and high pressures." *Can. Geotech. J.*, 54(2), 207-218.

Igarashi, S., Bentur, A., and Mindess, S., (1996). “Microhardness testing of cementitious materials,” *Adv. Cem. Based Mater.*, 4, 48–57.

Jin, Y. F., Yin, Z. Y., Wu, Z. X., and Daouadji, A. (2018a). “Numerical modeling of pile penetration in silica sands considering the effect of grain breakage.” *Finite Elem. Anal. Des.*, 144, 15–29.

Jin, Y. F., Yin, Z. Y., Wu, Z. X., and Zhou, W. H. (2018b). “Identifying parameters of

497 easily crushable sand and application to offshore pile driving." *Ocean Eng*., 154,
498 416-429.
499 Jin, Y. F., Yin Z. Y., Zhou, W. H., Yin, J. H., Shao, J. F. (2019). "A single-objective EPR
500 based model for creep index of soft clays considering L2 regularization." *Eng.*
501 *Geol.*, 248(8), 242-255.
502 Karatza, Z., Andò, E., Papanicolopulos, S. A., Ooi, J. Y., and Viggiani, G. (2017).
503 "Evolution of deformation and breakage in sand studied using X-ray tomography."
504 *Géotechnique*, 1, 1-11.
505 Karimpour, H., and Lade, P. V. (2010). "Time effects relate to crushing in sand." *J.*
506 *Geotech. Geoenviron.*, 136(9), 1209-1219.
507 Kikkawa, N., Pender, M. J., Orense, R. P., StGeorge, J. D., and Matsushita, E. (2011).
508 "K_0 Compression and Stress Relaxation of Pumice Sand." *J. Geotech. Geoenviron.*,
509 138(5), 625-628.
510 Kumara, G. H. A., Hayano, K., & Ogiwara, K. (2012). "Image analysis techniques on
511 evaluation of particle size distribution of gravel." *Int. J. Geomate*, 3(1), 290-297.
512 Kwok, C. Y., and Bolton, M. D. (2013). "DEM simulations of soil creep due to particle
513 crushing." *Géotechnique*, 63(16), 1365.
514 Lade, P. V., and Karimpour, H. (2010). "Static fatigue controls particle crushing and
515 time effects in granular materials." Soils Found., 50(5), 573-583.
516 Lade, P. V., and Karimpour, H. (2014). "Stress relaxation behavior in Virginia Beach
517 sand." *Can. Geotech. J.*, 52(7), 813-835.
518 Lade, P. V., and Karimpour, H. (2016). "Stress drop effects in time dependent behavior
519 of quartz sand." *Int. J. Solids Struct*., 87, 167-182.
520 Lee, I. K., and Coop, M. R. (1995). "The intrinsic behaviour of a decomposed granite
521 soil." *Géotechnique*, 45(1), 117-130.
522 Li, J., Huang, Y., Chen, Z., Li, M., Qiao, M., and Kizil, M. (2018). "Particle-Crushing
523 Characteristics and Acoustic-Emission Patterns of Crushing Gangue Backfilling
524 Material under Cyclic Loading." *Minerals*, 8(6), 244.

525 Lv, Y., Li, F., Liu, Y., Fan, P., and Wang, M. (2016). “Comparative study of coral sand
526 and silica sand in creep under general stress states.” *Can. Geotech. J.*, 54(11),
527 1601-1611.
528 Manso, J., Marcelino, J., and Caldeira, L. (2018). “Crushing and oedometer
529 compression of rockfill using DEM.” *Comput. Geotech.*, 101, 11-22.
530 McDowell, G. R., and de Bono, J. P. (2013). “A new creep law for crushable aggregates.”
531 *Géotech. Lett*, 3(3), 103-107.
532 McDowell, G. R., de Bono, J. P., Yue, P., and Yu, H. S. (2013). “Micro mechanics of
533 isotropic normal compression.” *Géotech. Lett.*, 3(4), 166-172.
534 Oldecop, L. A., and Alonso, E. E. (2007). “Theoretical investigation of the time-
535 dependent behaviour of rockfill.” *Géotechnique*, 57 (3), 289-301.
536 Ovalle, C., Dano, C., Hicher, P. Y., and Cisternas, M. (2014). “Experimental framework
537 for evaluating the mechanical behavior of dry and wet crushable granular materials
538 based on the particle breakage ratio.” *Can. Geotech. J.*, 52(5), 587-598.
539 Salami, Y., Dano, C., and Hicher, P. Y. (2017). “Infrared thermography of rock fracture.”
540 *Géotech. Lett.*, 7(1), 36-40.
541 Samsonov, G. V. (2012). “Handbook of the Physicochemical Properties of the
542 Elements.” Springer Science &Business Media.
543 Shi, X. S., and Herle, I. (2017). Numerical simulation of lumpy soils using a hypoplastic
544 model. *Acta Geotech.*, 12(2), 349-363.
545 Shi, X. S., Herle, I., and Muir Wood, D. (2018a). A consolidation model for lumpy
546 composite soils in open-pit mining. *Géotechnique*, 68(3), 189-204.
547 Shi, X. S., Yin, J. H., and Zhao, J. D. (2018b). An elastic visco-plastic model for binary
548 sand-clay mixtures with applications to one-dimensional finite strain consolidation
549 analysis. *J Eng. Mech.*
550 Silvani, C., Désoyer, T., and Bonelli, S. (2009). “Discrete modelling of time-dependent
551 rockfill behaviour.” *Int. J. Numer. Anal. Met.*, 33(5), 665-685.
552 Takei, M., Kusakabe, O., and Hayashi, T. (2001). “Time-dependent behavior of

553 crushable materials in one-dimensional compression tests.” *Soils Found.*, 41(1),
554 97-121.
555 Ueng, T. S., and Chen, T. J. (2000). "Energy aspects of particle breakage in drained
556 shear of sands." *Géotechnique*, 50(1), 65-72.
557 Wang, L, Z., Yin, Z. Y. (2015). “Stress-dilatancy of natural soft clay under undrained
558 creep condition.” *Int. J. Geomech.*, 15(5), A4014002.
559 Xiao, Y., Liu, H. (2017). “Elastoplastic constitutive model for rockfill materials
560 considering particle breakage.” *Int. J. Geomech.*, 17(1), 04016041.
561 Xiao, Y., Long, L., Evans, T. M., Zhou, H., Liu, H., and Stuedlein, A. W. (2019a).
562 “Effect of particle shape on stress-dilatancy responses of medium-dense sands.” *J.*
563 *Geotech. Geoenviron. Eng*., 145 (2), 04018105.
564 Xiao, Y., Meng, M., Daouadjie, A., Chen, Q., Wu, Z., and Jiang, X. (2019b). "Effect of
565 particle size on crushing and deformation behaviors of rockfill materials."
566 *Geoscience Frontiers*, https://doi.org/10.1016/j.gsf.2018.1010.1010.
567 Xiong, H, Nicot, F, and Yin, Z Y. (2017). “A three-dimensional micromechanically
568 based model.” *Int. J. Numer. Anal. Methods Geomech.*, 41(17), 1669-1686.
569 Xiong, H, Nicot, F, and Yin, Z. (2018). “From micro scale to boundary value problem:
570 using a micromechanically based model.” *Acta Geotech.*,
571 https://doi.org/10.1007/s11440-018-0717-7
572 Xu, D. S., Liu, H. B., Rui, R., and Gao, Y. (2019). “Cyclic and postcyclic simple shear
573 behavior of binary sand-gravel mixtures with various gravel contents.” *Soil Dyn.*
574 *Earthq. Eng.*, 123, 230-241.
575 Xu, D. S., Tang, Z. Y., and Zhang, L. (2019). “Interpretation of coarse effect in simple
576 shear behavior of binary sand-gravel mixture by DEM with authentic particle
577 shape.” *Constr. Build. Mater.*, 195, 292-304.
578 Xuan, D. X., Shui Z. H., and Wu, S. P. (2009). “Influence of silica fume on the
579 interfacial bond between aggregate and matrix in near-surface layer of concrete.”
580 *Constr. Build. Mater.*, 23(7), 2631-2635.

581 Xuan, D. X., Zhan, B. J. and Poon, C. S. (2016). “Assessment of Mechanical Properties
582 of Concrete Incorporating Carbonated Recycled Concrete Aggregates.” *Cement*
583 *Concrete Comp.*, 65, 67-74.
584 Yamamuro, J. A., Bopp, P. A., and Lade, P. V. (1996). “One-dimensional compression
585 of sands at high pressures.” *J. Geotech. Engrg*., 122(2), 147-154.
586 Yin, J. H., and Graham, J. (1994). “Equivalent times and one-dimensional elastic
587 viscoplastic modelling of time-dependent stress–strain behaviour of clays.” *Can.*
588 *Geotech. J.*, 31(1), 42–52.
589 Yin, Z. Y., Hicher, P. Y., Dano, C., and Jin, Y. F. (2017a). “Modeling mechanical
590 behavior of very coarse granular materials.” *J. Eng. Mech.*, 143(1), C4016006.
591 Yin, Z. Y., Jin, Y. F., Shen, S. L., and Huang, H. W. (2017b). “An efficient optimization
592 method for identifying parameters of soft structured clay by an enhanced genetic
593 algorithm and elastic–viscoplastic model.” *Acta Geotech*, 12(4), 849-867.
594 Yin, Z. Y., Karstunen, M., Chang, C. S., Koskinen, M., and Lojander, M. (2011).
595 “Modeling time-dependent behavior of soft sensitive clay.” *J. Geotech.*
596 *Geoenviron. Eng*, 137(11), 1103-1113.
597 Yin, Z. Y., Yin, J. H., and Huang, H. W. (2015). “Rate-dependent and long-term yield
598 stress and strength of soft Wenzhou marine clay: experiments and modeling.” *Mar.*
599 *Georesour. Geotec*., 33(1), 79-91.
600 Yin, Z. Y., Zhu, Q. Y., Yin, J. H., and Ni, Q. (2014). “Stress relaxation coefficient and
601 formulation for soft soils.” *Géotech. Lett.*, 4(1), 45-51.
602 Zhan, B. J., Xuan, D. X., and Poon, C. S. (2018). “Enhancement of recycled aggregate
603 properties by accelerated CO2 curing coupled with limewater soaking process.”
604 *Cement Concrete Comp.*, 89, 230-237.
605 Zhou, B., Wang, J., and Wang, H. (2018). “Three-dimensional sphericity, roundness
606 and fractal dimension of sand particles.” *Géotechnique*, 68(1), 18-30.
607 Zhu, Q. Y., Yin Z. Y., Hicher, P. Y., and Shen, S. L. (2016). “Nonlinearity of one-
608 dimensional creep characteristics of soft clays.” *Acta Geotech.*, 11(4), 887-900.

Table 1. List of CRS and MLO tests

Test Name.	Initial void ratio (e_0)	Test condition
CRS_Dry	0.847	Compressed and unloaded-reloaded at constant $\dot{\varepsilon}$ of 2%/h at 0.5, 0.8, and 1.5 MPa, started relaxation at 2 MPa
CRS_Sat	0.851	Compressed and unloaded-reloaded at $\dot{\varepsilon}$ of 2%/h at 0.5 MPa, compressed and unloaded-reloaded at $\dot{\varepsilon}$ of 0.2%/h at 0.6 MPa, compressed and unloaded-reloaded at 0.9 MPa at $\dot{\varepsilon}$ of 20%/h, compressed at $\dot{\varepsilon}$ of 2%/h to 2 MPa, started relaxation at 2 MPa
CRS_Flo1	0.865	Compressed at $\dot{\varepsilon}$ of 2%/h to 0.5 MPa, compressed at $\dot{\varepsilon}$ of 0.2%/h to 0.7 MPa, compressed at $\dot{\varepsilon}$ of 20%/h to 1.2 MPa, compressed at $\dot{\varepsilon}$ of 20%/h to 2 MPa, started relaxation at 2 MPa, flooded specimen just at the start of relaxation
CRS_Flo2	0.858	Compressed at $\dot{\varepsilon}$ of 2%/h, started relaxation at 0.5, 0.8 MPa, compressed at $\dot{\varepsilon}$ of 2%/h to 2 MPa, started relaxation at 2 MPa, flooded after 1 hour of relaxation
MLO_Dry	0.856	Step-wisely loaded to 0.5 MPa, creeped for 12 hours, step-wisely loaded to 2 MPa, creeped for 12 hours
MLO_Sat	0.859	Step-wisely loaded to 0.5 MPa, creeped for 12 hours, step-wisely loaded to 2 MPa, creeped for 12 hours
MLO_Flo	0.854	Step-wisely loaded to 0.5 MPa, creeped for 12 hours, flooded after 1 hour of creep, step-wisely loaded to 2 MPa, creeped for 12 hours

Table 2. List of formulas of shape descriptors

Descriptor	Formula	Parameters
Circularity	$\frac{4\pi A}{P^2}$	A is the area of particle in square pixels or in calibrated square units; P is the length of the outside boundary of the particle
Aspect ratio	$\frac{L_{major}}{L_{minor}}$	L_{major} is the major axis of particle's fitted ellipse; L_{minor} is the minor axis of particle's fitted ellipse
Roundness	$\frac{4A}{\pi L_{major}{}^2}$	A is the area of particle in square pixels or in calibrated square units; L_{major} is the major axis of particle's fitted ellipse
Solidity	$\frac{A}{A_{hull}}$	A is the area of particle in square pixels or in calibrated square units; A_{hull} is the area of convex hull

Table 3. List of plastic work and breakage ratio of each specimen

Test Name.	$W_{p,d}$ (kPa)	$W_{p,w}$ (kPa)	$W_{p,e}$ (kPa)	B_r determined by Eq. (1)	Calculated B_r by fitted Eq. (2)
CRS_Dry	86.2	0	86.2	0.203	0.212
CRS_Sat	0	164.3	164.3	0.481	0.485
CRS_Flo1	99.9	10.3	64.7	0.310	0.271
CRS_Flo2	86.6	150.9	198.0	0.267	0.280
MLO_Dry	124.2	0	124.2	0.523	0.501
MLO_Sat	0	174.9	174.9	0.544	0.534
MLO_Flo	9.5	194.4	199.6	0.490	0.532

Figure 1

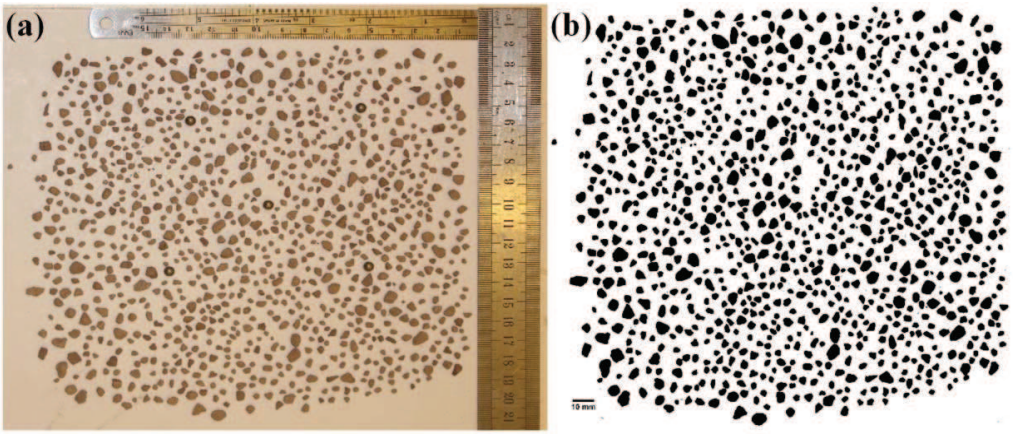

Figure 2

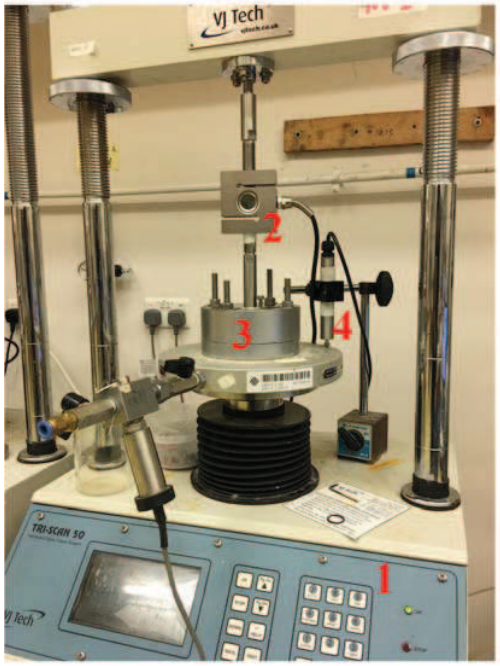

(a)

1. **Triaxial loading frame**
2. **S-beam load cell**
3. **Oedometer ring**
4. **Vertical LVDT**

(b)

1. **Hanger**
2. **Vertical LVDT**
3. **Chamber**
   (Oedometer ring inside)
4. **Lever arm**

Figure 3

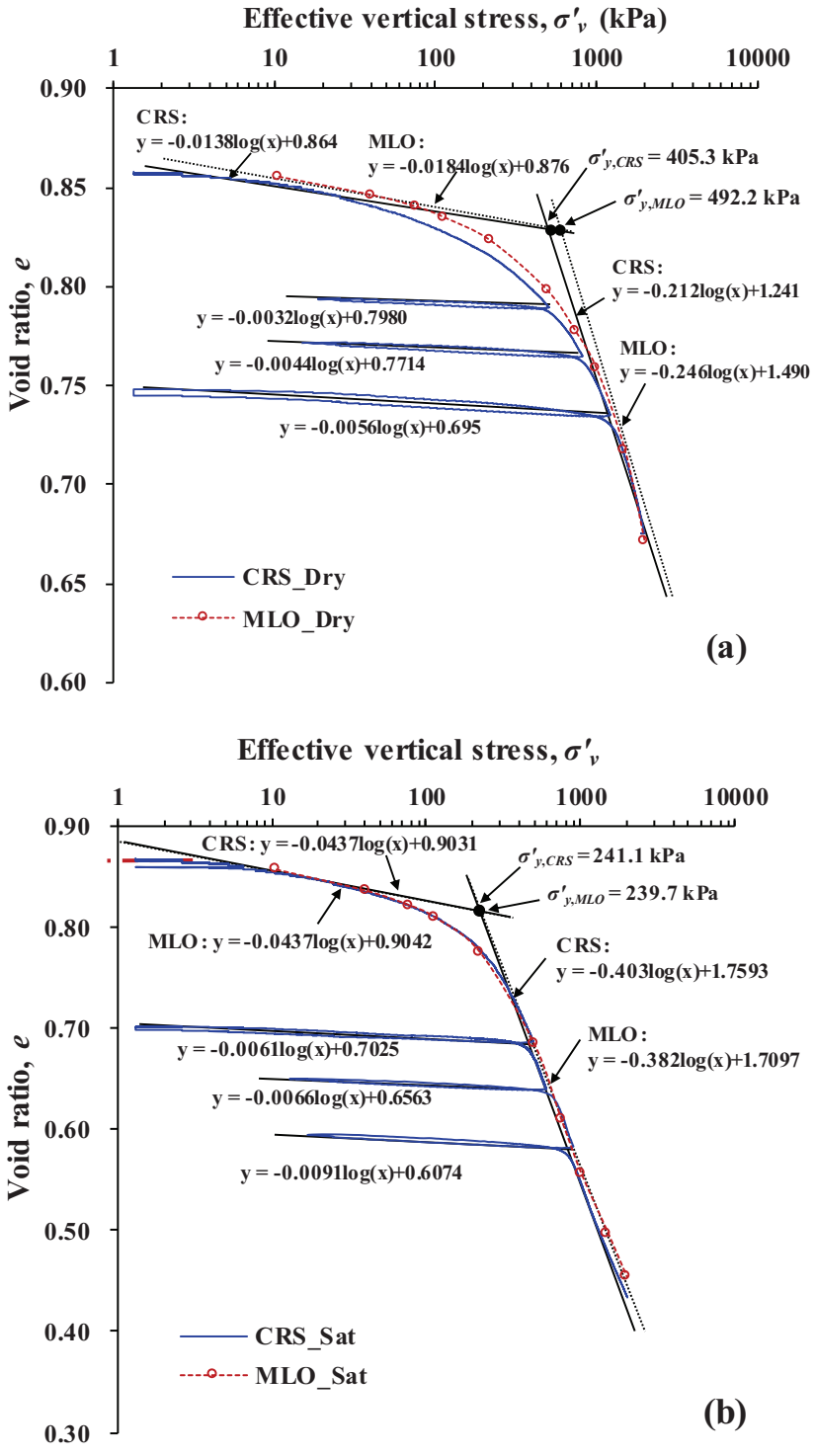

Figure 4

Click here to access/download;Figure;Figure 4.eps

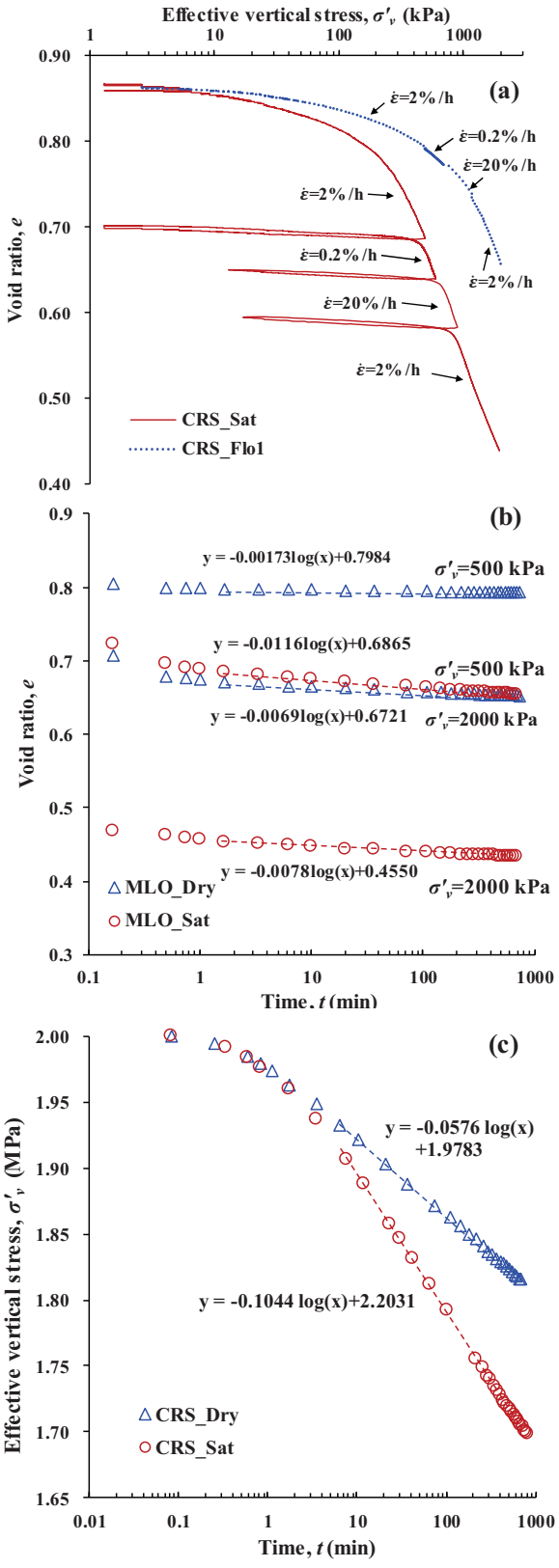

Figure 5 (a)

Click here to access/download;Figure;Figure 5(a).eps

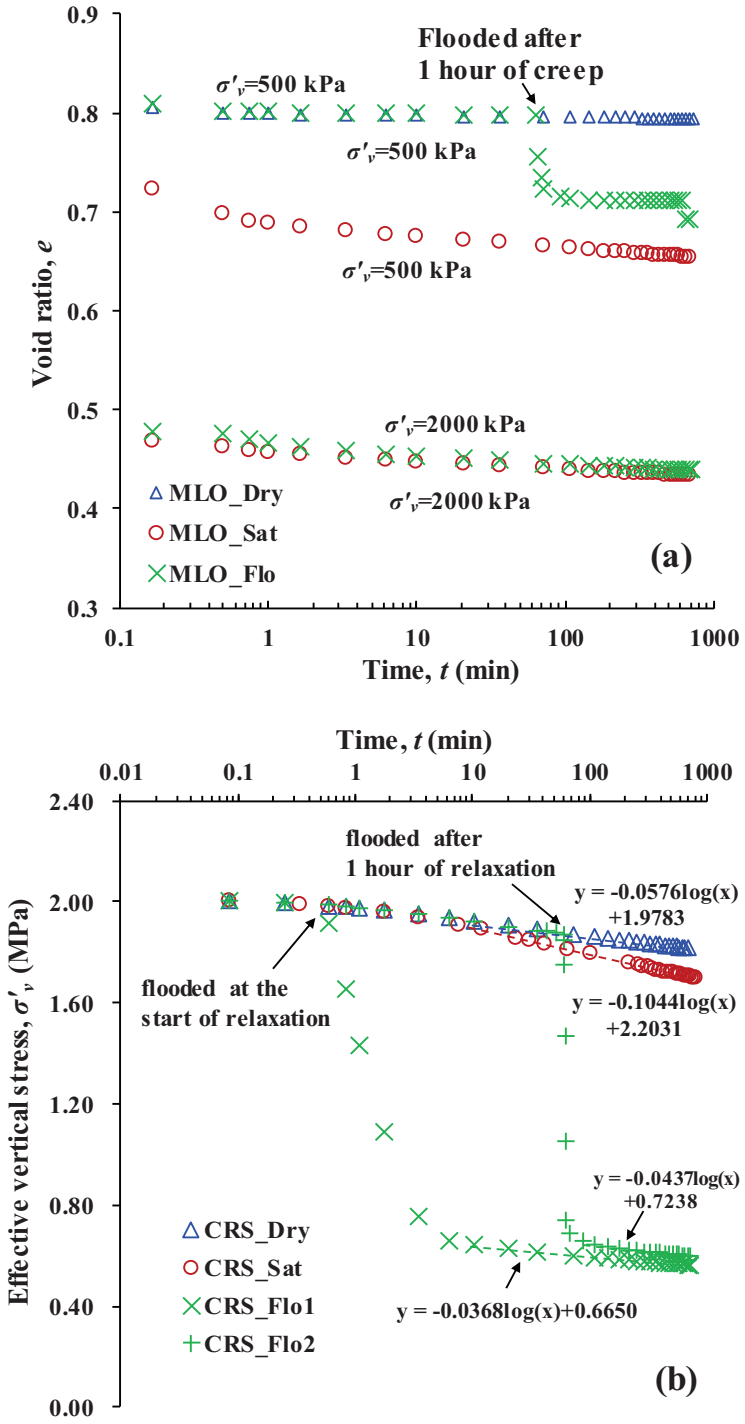

Figure 5 (b)

Click here to access/download;Figure;Figure 5(b).eps

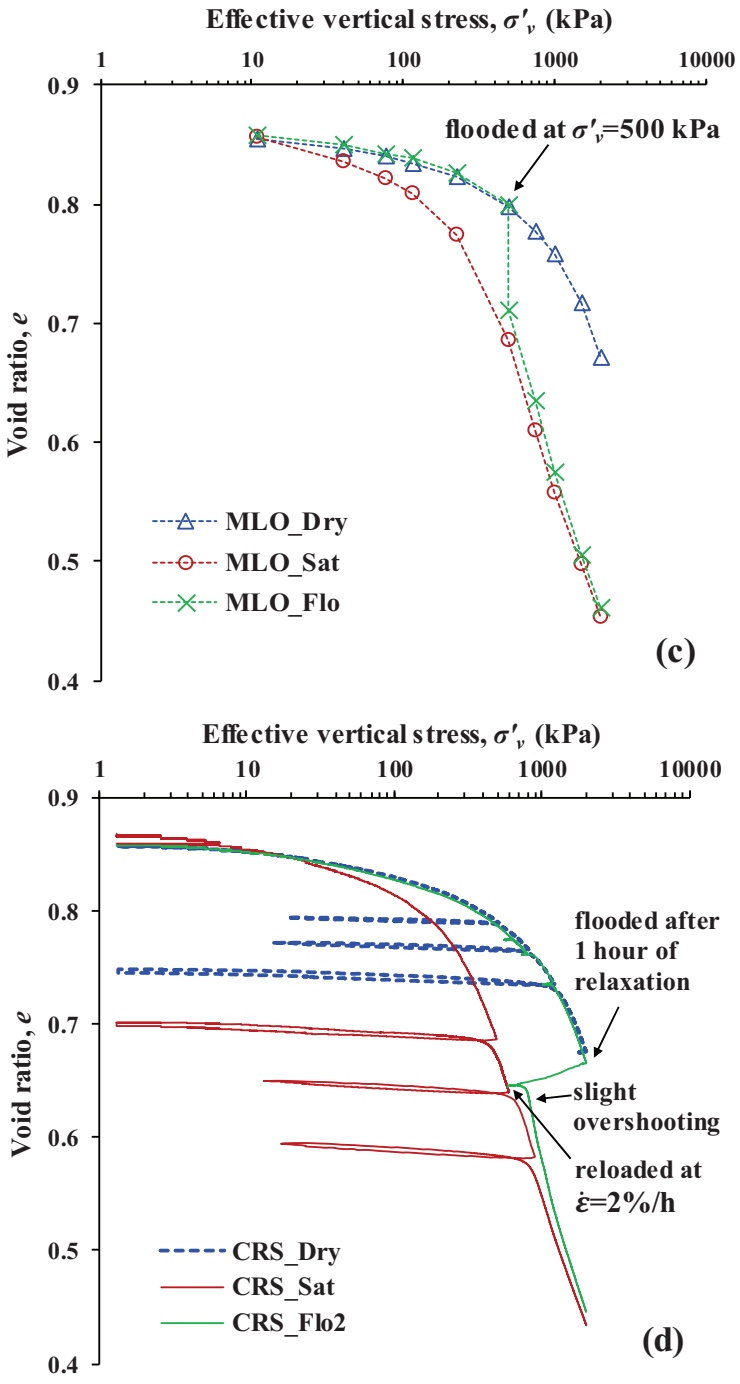

Figure 6

Click here to access/download;Figure;Figure 6.eps

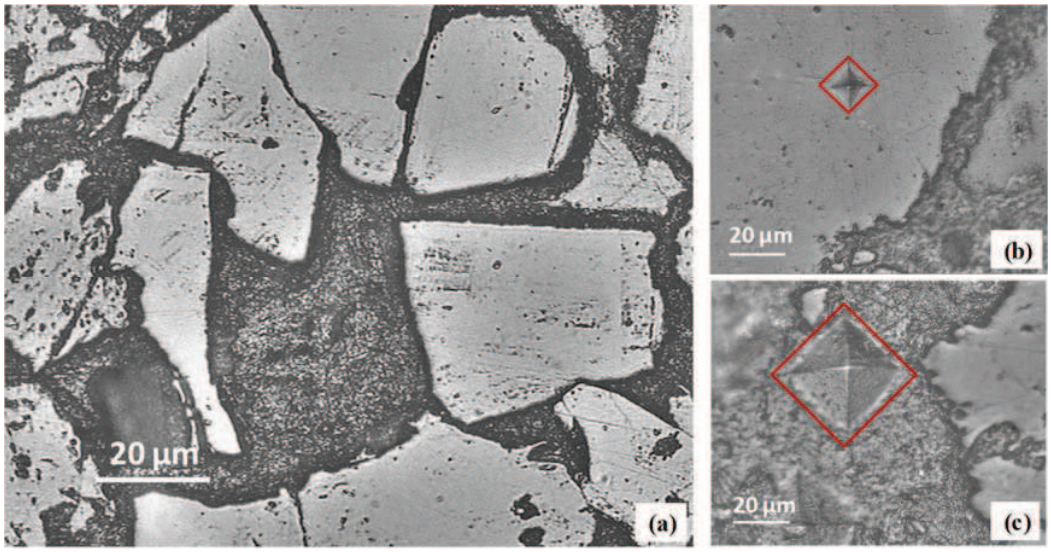

Figure 7

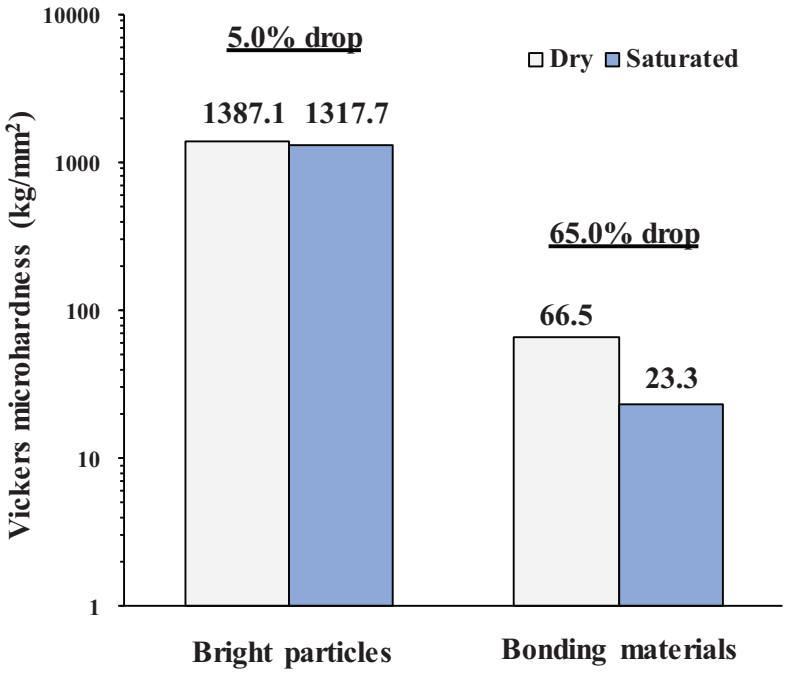

Figure 8

Click here to access/download;Figure;Figure 8.eps

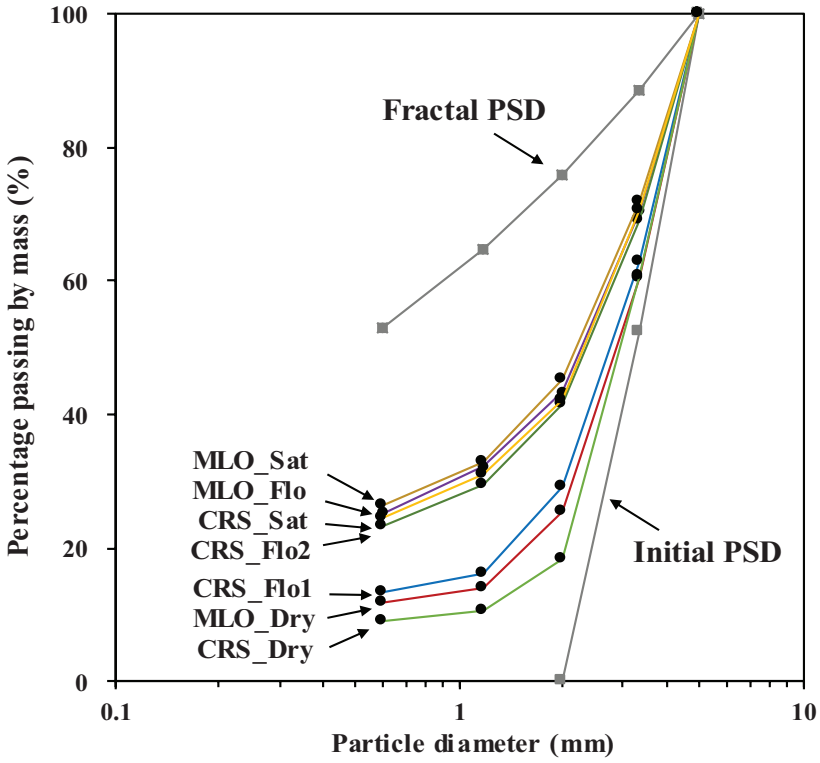

Figure 9

Click here to access/download;Figure;Figure 9.eps

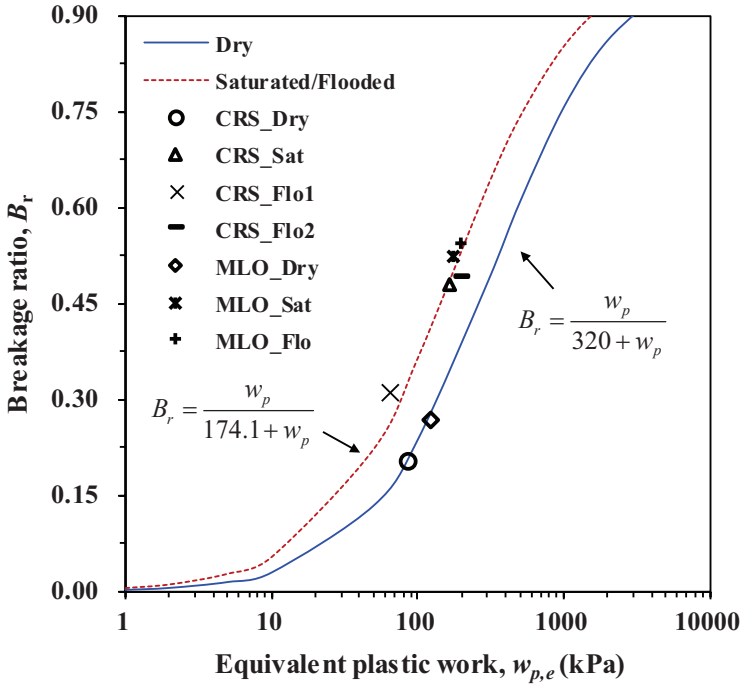

Figure 10

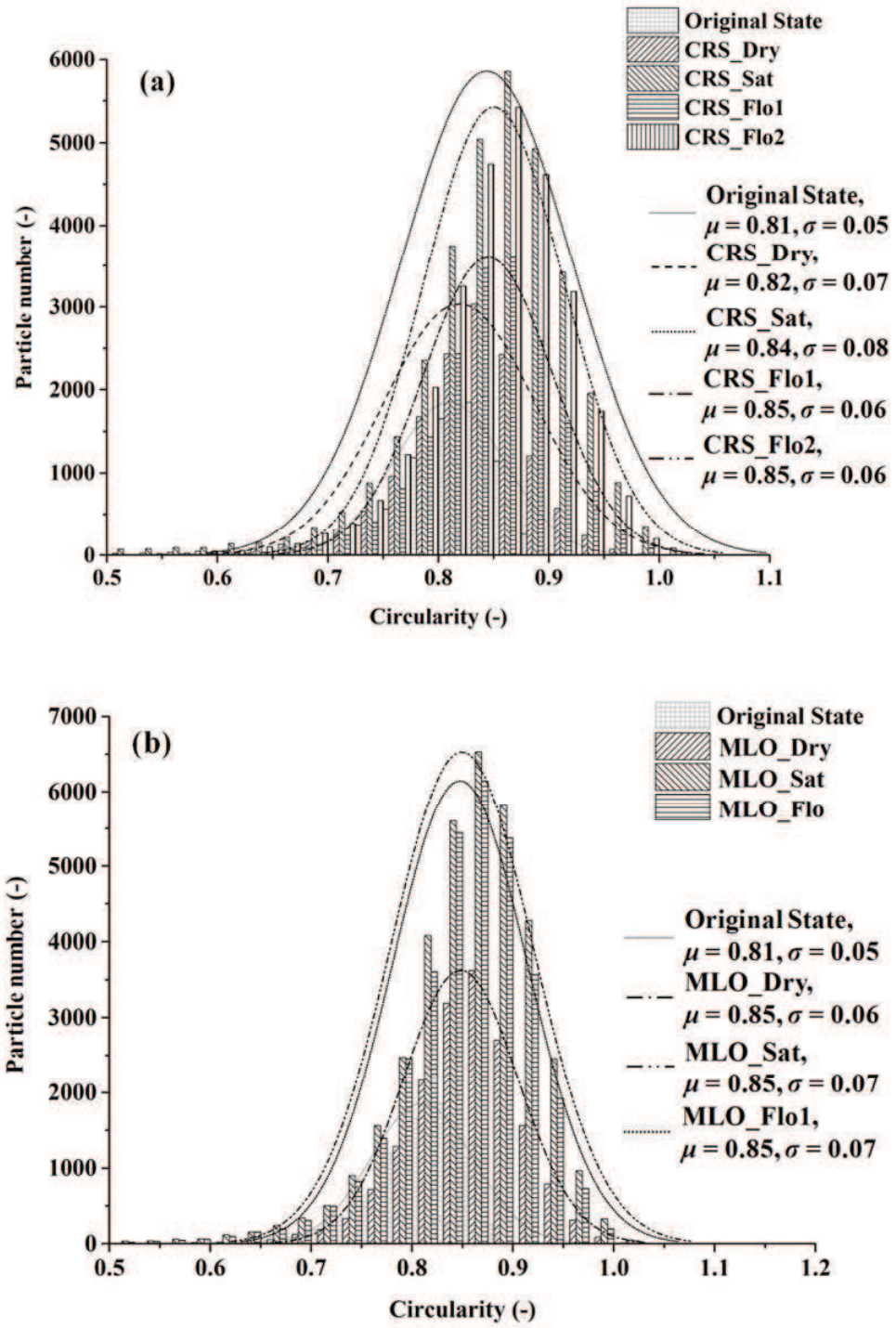

Figure 11

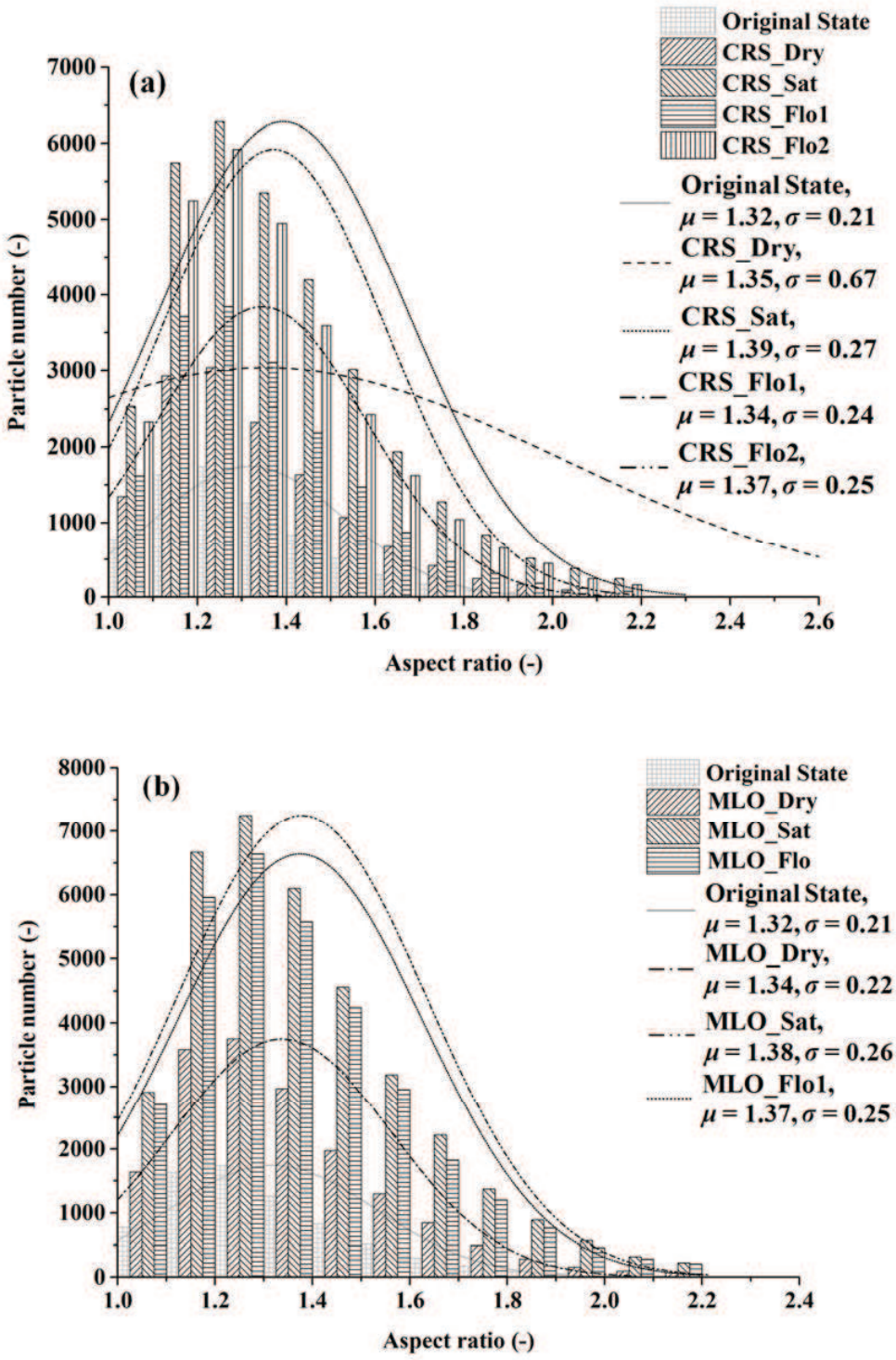

Figure 12

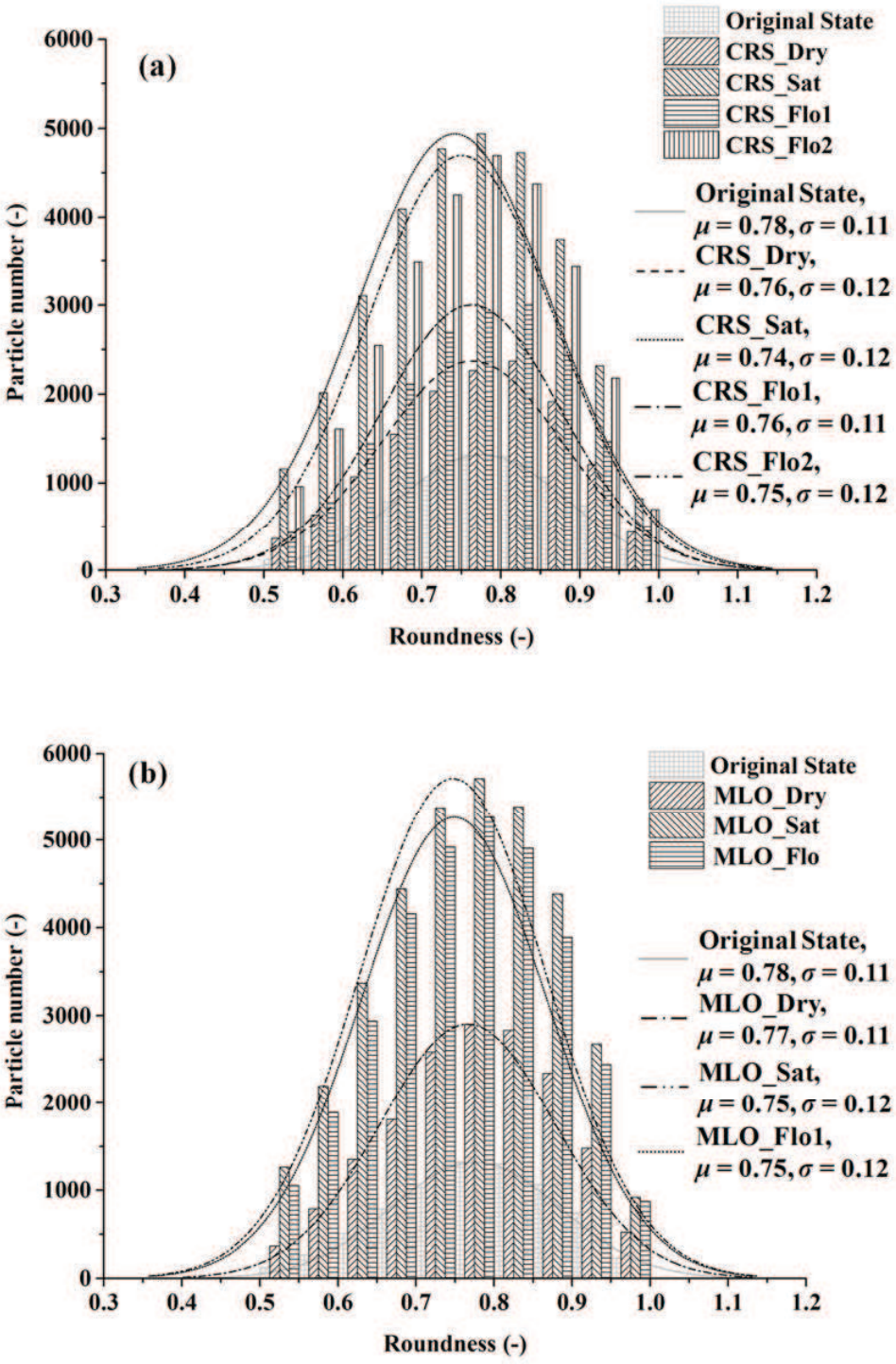

Figure 13

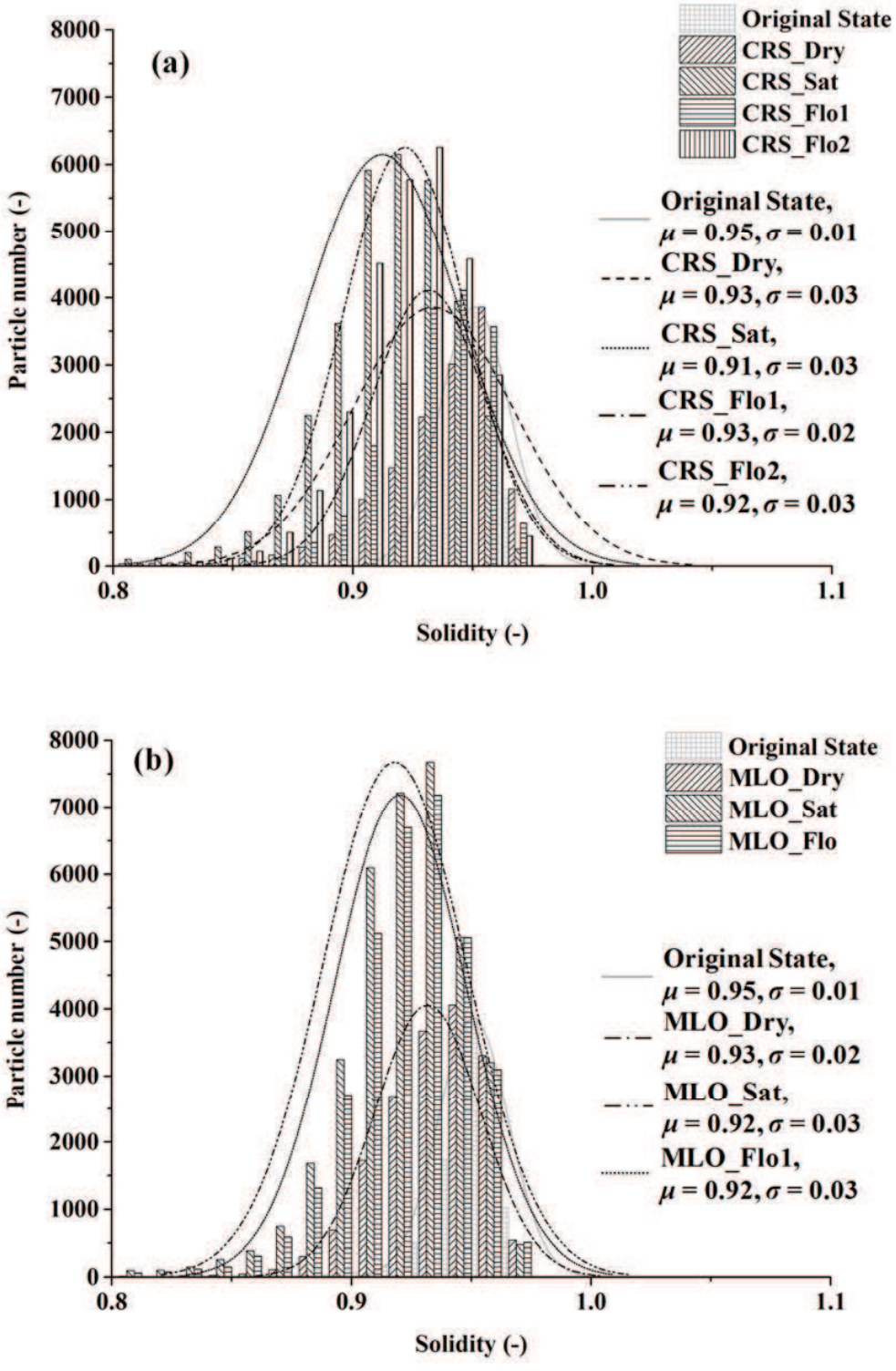

Figure caption list